Triple oxygen isotope insight into terrestrial pyrite oxidation

Jordon D. Hemingway[a,1], **Haley Olson**[a], **Alexandra V. Turchyn**[b], **Edward T. Tipper**[b], **Mike Bickle**[b], **and David T. Johnston**[a]

[a]Department of Earth and Planetary Sciences, Harvard University, Cambridge, MA 02138; [b]Department of Earth Sciences, Cambridge University, Cambridge, UK CB2 1TN

This manuscript was compiled on January 26, 2020

The mass-independent minor oxygen isotope compositions ($\Delta'^{17}O$) of atmospheric O_2 and CO_2 are primarily regulated by their relative partial pressures, pO_2/pCO_2. Pyrite oxidation during chemical weathering on land consumes O_2 and generates sulfate that is carried to the ocean by rivers. The $\Delta'^{17}O$ values of marine sulfate deposits have thus been proposed to quantitatively track ancient atmospheric conditions. This proxy assumes direct O_2 incorporation into terrestrial pyrite oxidation-derived sulfate, but a mechanistic understanding of pyrite oxidation—including oxygen sources—in weathering environments remains elusive. To address this issue, we present sulfate source estimates and $\Delta'^{17}O$ measurements from modern rivers transecting the Annapurna Himalaya, Nepal. Sulfate in high-elevation headwaters is quantitatively sourced by pyrite oxidation, but resulting $\Delta'^{17}O$ values imply no direct tropospheric O_2 incorporation. Rather, our results necessitate incorporation of oxygen atoms from alternative, ^{17}O-enriched sources such as reactive oxygen species. Sulfate $\Delta'^{17}O$ decreases significantly when moving into warm, low-elevation tributaries draining the same bedrock lithology. We interpret this to reflect overprinting of the pyrite oxidation-derived $\Delta'^{17}O$ anomaly by microbial sulfate reduction and reoxidation, consistent with previously described major sulfur and oxygen isotope relationships. The geologic application of sulfate $\Delta'^{17}O$ as a proxy for past pO_2/pCO_2 should consider both (i) alternative oxygen sources during pyrite oxidation and (ii) secondary overprinting by microbial recycling.

atmospheric O_2 | chemical weathering | $\Delta'^{17}O$ | Himalayas | sulfur cycle

Atmospheric molecular oxygen (O_2) governs biogeochemical cycles, Earth's surface redox state, and the evolution of life; O_2 partial pressure (pO_2) has increased drastically in the geologic past in response to biologic and geologic drivers (1, 2). Despite this importance, quantitatively constraining pO_2 throughout Earth's history remains challenging due to a lack of direct proxies (2). Recently, the minor oxygen isotope composition ($^{17}O/^{16}O$, reported as $\Delta'^{17}O$; Materials and Methods) of geologically preserved minerals has been proposed as one such proxy (1, 3–8). This approach utilizes the fact that photochemical reactions between O_2, ozone (O_3), and carbon dioxide (CO_2) in the stratosphere generate anomalous, mass-independent ^{17}O signatures that are mixed into the troposphere (9). In particular, tropospheric O_2 carries a large negative $\Delta'^{17}O$ anomaly, the magnitude of which reflects: (i) the ratio of O_2 to CO_2 partial pressures (pO_2/pCO_2), which determines the strength of the signal acquired during stratospheric photochemistry, and (ii) the amount of O_2 generated by oxygenic photosynthesis in the biosphere, which dilutes stratospheric inputs (1, 6). Thus, if pCO_2 and biospheric productivity can be independently constrained, then tropospheric O_2 $\Delta'^{17}O$ is potentially a direct and quantitative pO_2 tracer.

Sulfate (SO_4^{2-}) bearing minerals are particularly attractive reservoirs for this method of reconstructing pO_2 in the geologic past because oxidative pyrite (FeS_2) weathering consumes O_2 (10, 11). If oxidation of pyrite contained in exhumed sedimentary rocks on land follows the reaction:

$$FeS_2 + \frac{7}{2}\,O_2 + H_2O \longrightarrow Fe^{2+} + 2\,SO_4^{2-} + 2\,H^+, \qquad [1]$$

then contemporaneous tropospheric O_2—including its anomalous ^{17}O composition—could be directly incorporated into resulting sulfate (12). Isotopically labeled oxidation experiments support this idea; ≈8 % to 15 % of sulfate oxygen atoms have been shown to be sourced directly from dissolved O_2 under well-oxygenated experimental conditions (12, 13). In light of these results and the fact that sulfate oxygen isotopes do not equilibrate with water on geologically relevant timescales, preserved barite ($BaSO_4$), gypsum ($CaSO_4$), and carbonate-associated sulfate $\Delta'^{17}O$ values have been used to reconstruct pO_2/pCO_2 throughout Earth's history (3–8, 14, 15). Such interpretations require two criteria to be met: (i) this direct O_2 consumption mechanism (Eq. 1) contributes a significant proportion of pyrite oxidation-derived sulfate and (ii) primary $\Delta'^{17}O$ signals are not overprinted or diluted in the environment prior to being preserved in the rock record. Tropospheric O_2 ^{17}O compositions in the geologic past are thus typically reconstructed using the most negative sulfate $\Delta'^{17}O$ value from a given geologic unit (i.e., least overprinted) and scaling by a ≈8 % to 15 % O_2 incorporation factor (7, 15).

However, anoxic laboratory experiments and modern field observations complicate this picture. Specifically, both biotic

Significance Statement

Pyrite is oxidized during weathering to form dissolved sulfate that is carried to the ocean by rivers. This process is thought to incorporate atmospheric O_2-derived oxygen; geologically preserved sulfate has thus been proposed to directly trace past O_2 isotope compositions. However, this mechanism has not been thoroughly tested in modern weathering environments. We show that dissolved sulfate in Himalayan rivers is predominantly derived from pyrite, yet its oxygen isotope compositions preclude direct O_2 incorporation. Rather, alternative oxygen sources (e.g., reactive oxygen species) may be incorporated during oxidation, prompting reconsideration of the pyrite oxidation mechanism and the interpretation of geologically preserved sulfate as a direct O_2 tracer.

Author contributions: J.D.H and D.T.J. designed research; J.D.H. and H.O performed research; A.V.T., E.T.T. and M.B. contributed new reagents or analytic tools; J.D.H., H.O. and D.T.J. analyzed data; J.D.H., H.O., A.V.T., E.T.T., M.B., and D.T.J. wrote the paper.

The authors declare no conflict of interest.

[1]To whom correspondence should be addressed. E-mail: jordon_hemingwayfas.harvard.com

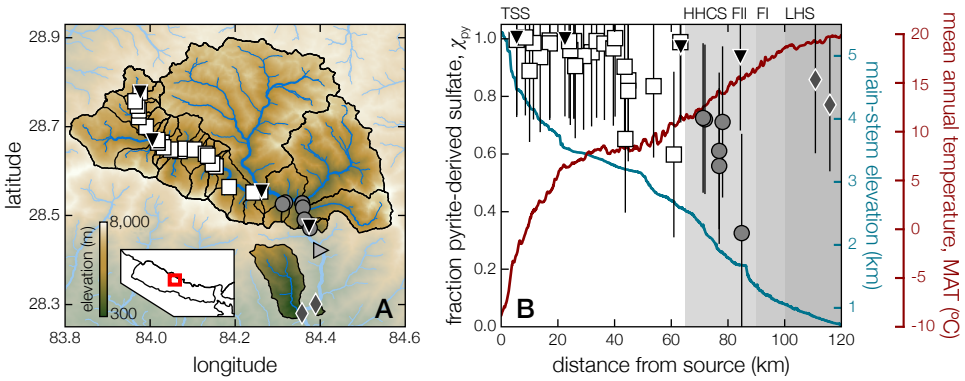

Fig. 1. (*A*) Marsiyandi basin map. Black lines delineate catchment areas upstream of each sample location. Background color represents elevation. Inset shows study location within Nepal. (*B*) Downstream evolution of elevation (blue line) and local MAT (red line) moving along the main-stem Marsiyandi. Also shown is the estimated fraction of sulfate derived from pyrite oxidation (χ_{py}) for each sample; tributaries are plotted at their confluence with the main-stem. Background shading indicates bedrock lithology. Symbols refer to: TSS tributaries (white squares), HHCS FII tributaries (gray circles), HHCS FI tributaries (light gray triangles), LHS tributaries (dark gray diamonds), and main-stem Marsiyandi (black triangles).

and abiotic experiments (10, 11, 13, 16, 17) imply that sulfate oxygen can be quantitatively sourced from meteoric water:

$$FeS_2 + 14\,Fe^{3+} + 8\,H_2O \longrightarrow 15\,Fe^{2+} + 2\,{SO_4}^{2-} + 16\,H^+. \quad [2]$$

O_2 is then consumed indirectly during subsequent oxidation of Fe^{2+} to Fe^{3+}. If pyrite oxidation in the environment exclusively follows Eq. 2, then product sulfate $\Delta'^{17}O$ is decoupled from atmospheric pO_2/pCO_2. Recent studies using major oxygen and sulfur isotope compositions ($\delta^{18}O$, $\delta^{34}S$; Materials and Methods) suggest that pyrite oxidation in some modern river systems occurs in suboxic groundwater aquifers and quantitatively incorporates meteoric water-derived oxygen (18–20). Consistent with this interpretation, detailed studies of shale bedrock drill cores indicate that pyrite oxidation occurs in low-O_2 pores and microfractures within a deep, sharp reaction front independent of erosion rate (21). Such results raise the question as to why direct O_2 incorporation into sulfate is evident in the geologic past but is apparently absent from modern pyrite weathering environments. Furthermore, pyrite oxidation must proceed via 1-electron transfer steps regardless of the exact mechanism involved (11, 22, 23), raising the possibility that reactive oxygen species (ROS; e.g., H_2O_2, $O_2^{\bullet-}$, $OH^{\bullet}$) may provide additional, isotopically unique oxygen sources to sulfate (24, 25). ROS incorporation could help to reconcile modern and ancient observations, but its environmental importance remains unknown.

To provide new insight, we constrain the sulfate budget in a suite of highly erosive mountainous rivers. Building upon previous work reporting $\delta^{18}O$ and $\delta^{34}S$ evolution (20), we document sulfate source and $\Delta'^{17}O$ values for samples collected throughout the Marsiyandi River basin, Annapurna Himalaya, Nepal. These results update our understanding of fluvial sulfate oxygen isotope systematics, with implications for modern weathering budgets and geologic pO_2/pCO_2 reconstructions.

Study Setting. The Marsiyandi River is located in the Southern Flank of the Annapurna Himalaya, Central Nepal (Fig. 1A). Headwaters drain the Tethyan Sedimentary Series (TSS); although some Manaslu granite exposures exist within our study region, bedrock is primarily described as a continental margin sequence containing variably metamorphosed limestone and siliclastics with interbedded pyrite-rich black shales (26–28). The TSS lies entirely within the Himalayan orogenic rain shadow; vegetation is sparse (29) and mean annual precipitation (MAP) never exceeds 1000 mm yr^{-1} (average ≈500 mm yr^{-1}) (30). Mean annual temperature (MAT) within the TSS ranges from −10 °C in the highest elevations to near 15 °C in the lowest elevations (Fig. 1B). Downstream of the TSS, the Higher Himalayan Crystalline Series (HHCS) contains two main bedrock units: Formation I (FI), dominated by silicate gneiss, and Formation II (FII), dominated by calc-silicate metamorphic rocks (26, 31). MAP increases markedly due to the influence of the Indian Summer Monsoon, reaching 2500 mm yr^{-1} (30), whereas MAT exhibits only modest increases (Fig. 1B). Further downstream, the Lesser Himalayan Series (LHS) is described as undifferentiated low- to medium-grade metasedimentary and metavolcanic rocks (27) and by MAP and MAT values near those within the HHCS. Importantly, evaporitic successions have never been reported in Central Nepal (29)*.

Results

Samples were collected in May (pre-monsoon) and September (monsoon season) 2002 across a ≈120 km transect starting at the Marsiyandi River headwaters in the TSS (5000 m elevation) and ending in the LHS near the base of the Himalaya (750 m elevation; Fig. 1B) (29, 33–35). Most samples were collected from small tributaries draining single lithologies (median catchment area = 20 km^2; Table S2) and are independent of one another. Tributaries span a range of catchment slopes (24.0 to 41.1 deg), MAP (407 to 1330 mm yr^{-1}), MAT (−10 to 15 °C), and glacial extent (0 to 46 % by area; Table S2). This approach allows us to isolate the effect of geomorphic/environmental changes on riverine chemistry while holding lithology and catchment area roughly constant (36). To investigate main-stem evolution, we additionally report results from the Marsiyandi River at 4 locations throughout the basin.

Sulfate Sources. Sulfate source contributions—including atmospheric inputs and carbonate, evaporite, granite, and shale weathering—were estimated using a conservative tracer mixing model and previously published major ion concentrations (Materials and Methods) (29). Results indicate that the fraction of riverine sulfate derived from pyrite oxidation in shale, termed χ_{py}, ranges from 40 to 100 % (Fig. 1B). χ_{py} is highest in sulfate-rich TSS tributaries, ranging from 60 to 100 % and averaging 91 ± 11 % ($\mu \pm 1\sigma$, n = 25; Table S1). Slightly lower χ_{py} values in the most downstream TSS samples could result from partial HHCS or Manaslu granite bedrock exposure in these tributaries (29). Across the entire sample set,

* Chloride-rich hydrothermal hotsprings along fault zones do suggest the presence of basinal brines or buried halite (33, 37). However, hot springs are deficient in both SO_4^{2-} and Ca^{2+} relative to Cl^- and Na^+ (37), indicating minimal contribution of gypsum dissolution to hydrothermal solutes and thus precluding evaporite weathering as a major driver of observed sulfate trends.

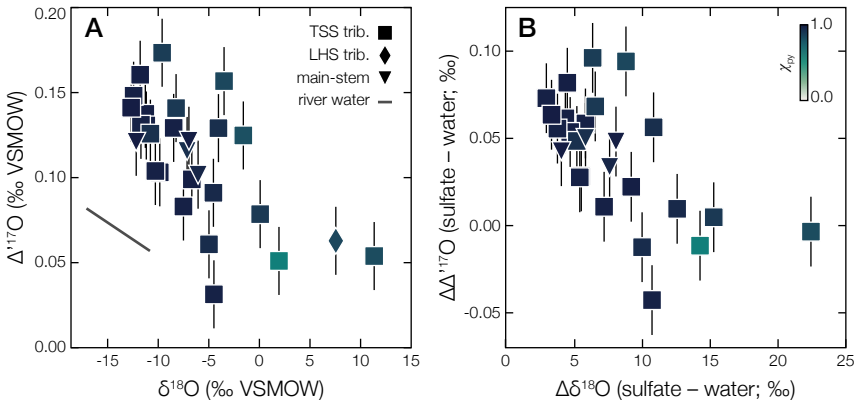

Fig. 2. Oxygen isotope compositions. (*A*) colored points: $\Delta'^{17}O$ vs. $\delta^{18}O$ scatter plot for all sulfate samples; gray line: Marsiyandi basin river water isotope array. Water $\delta^{18}O$ was measured directly (20) and $\Delta'^{17}O$ was calculated using the global meteoric water line (32). (*B*) Scatter plot of $\Delta\Delta'^{17}O$ vs. $\Delta\delta^{18}O$, the offsets between sulfate and concomitant river water $\Delta'^{17}O$ and $\delta^{18}O$ (Materials and Methods). For both panels, symbol colors refer to the estimated fraction of sulfate derived from pyrite oxidation (χ_{py}) and shapes represent: TSS tributaries (squares), LHS tributaries (diamonds), and the main-stem Marsiyandi (triangles). $\Delta'^{17}O$ and $\Delta\Delta'^{17}O$ uncertainty ($\mu \pm 1\sigma$) is the long-term instrument reproducibility (Materials and Methods); $\delta^{18}O$ and $\Delta\delta^{18}O$ uncertainty is smaller than marker points (20). Both panels show that sulfate is generally enriched in ^{17}O relative to meteoric water, opposite of what would be expected from direct atmospheric O_2 incorporation.

χ_{py} decreases moving downstream (slope $= -0.003\,\%\,km^{-1}$, $p = 6.5 \times 10^{-5}$), largely due to the sharp drop within tributaries draining HHCS FII calc-silicate metamorphic rocks. This drop coincides with the Southern Tibetan Detachment System and the Main Central Thrust (35) and is likely driven by contributions from limestone weathering in this region, as suggested by our weathering model results (Table S1). In contrast, when considering only TSS samples that are sufficiently upstream of potential HHCS and Manaslu granite influence ($\leq$40 km from the the source) (29), χ_{py} remains near 100 % and does not correlate with downstream distance ($p > 0.05$). Importantly, results account for precipitation-derived sulfate, including anthropogenic sources (i.e., acid rain). These inputs never exceed 11 % of total sulfate in any sample, averaging only 2.0 ± 2.5 % ($n = 38$) across the entire sample set and 1.0 ± 1.1 % ($n = 25$) within the TSS, consistent with low measured sulfate concentrations in Himalayan rain water (38, 39). We thus primarily limit our sulfate ^{17}O isotope measurements to upstream TSS catchments.

Sulfate Isotopes. Riverine sulfate $\Delta'^{17}O$ ranges from 0.041 to 0.180 ‰ VSMOW (average $= 0.117 \pm 0.038$ ‰ VSMOW; $n = 29$; Table S1) and exhibits a significant decrease moving downstream (slope $= -0.001$ ‰ km^{-1}; $p = 3.8 \times 10^{-3}$; $R^2 = 0.35$; Fig. S1). Sulfate $\Delta'^{17}O$ is negatively correlated with both $\delta^{18}O$ (slope $= -0.005$ ‰ ‰$^{-1}$; $p = 3.8 \times 10^{-3}$; $R^2 = 0.44$; Fig. 2A) and $\delta^{34}S$ (slope $= -0.002$ ‰ ‰$^{-1}$; $p = 1.6 \times 10^{-4}$; $R^2 = 0.41$; Table S1). Because sulfate oxygen can be sourced directly from water (Eq. 2) (10, 11, 16, 17, 40), we additionally report offsets between sulfate and concomitant river water $\delta^{18}O$ and $\Delta'^{17}O$, termed $\Delta\delta^{18}O$ and $\Delta\Delta'^{17}O$ (Fig. 2B; Materials and Methods). Water $\delta^{18}O$ was measured directly (20), whereas $\Delta'^{17}O$ was calculated using the global meteoric water line (32). $\Delta\Delta'^{17}O$ ranges from -0.033 to 0.103 ‰ (average $= 0.048 \pm 0.034$ ‰; $n = 26$; Table S1) and displays a statistically significant decrease with increasing $\Delta\delta^{18}O$ (slope $= -0.008$ ‰ ‰$^{-1}$; $p = 8.3 \times 10^{-4}$; $R^2 = 0.39$; Fig. 2B). In contrast, both $\Delta'^{17}O$ and $\Delta\Delta'^{17}O$ values do not correlate with χ_{py} estimates nor with estimated fractional dolomite, gneiss/granite, limestone, or evaporite end-member weathering contributions ($p > 0.05$). Unlike χ_{py}, which is largely stable near 100 % within the TSS, sulfate $\Delta'^{17}O$ values in tributaries draining this region display large and systematic decreases moving downstream (Fig. S1).

Discussion

Fluvial Sulfate Oxygen Source. We observe spatially coherent sulfate oxygen isotope signals throughout the Marsiyandi River basin. Headwater sulfate exhibits large, positive $\Delta'^{17}O$ values ($\Delta\Delta'^{17}O \approx 0.10$ ‰) as well as $\delta^{18}O$ near that of local meteoric water ($\Delta\delta^{18}O \leq 5$ ‰). Consistent with previous observations based on sulfate $\delta^{18}O$ from a suite of global rivers (18–20), these results imply that pyrite weathering in mountainous headwaters occurs primarily within suboxic groundwater aquifers. Sulfate ^{17}O compositions indicate no appreciable O_2 incorporation during pyrite oxidation (Eq. 1). Any O_2 contribution would produce sulfate with $\Delta'^{17}O$ *below* the meteoric water line (i.e., $\Delta\Delta'^{17}O < 0$) since $\Delta'^{17}O \approx -0.5$ ‰ VSMOW in modern tropospheric O_2 (6, 9). However, the opposite is observed (Fig. 2B). Furthermore, mass-dependent isotope fractionation associated with anoxic pyrite weathering (Eq. 2) likely cannot explain observed ^{17}O enrichment since this would require a mass law of $\theta \approx 0.54$ to 0.55, considerably higher than any known low-temperature microbial or abiotic processes (1, 41). Rather, positive $\Delta\Delta'^{17}O$ values require either (i) overprinting by atmospherically derived (precipitation or aerosol) sulfate inputs (1, 41) or (ii) an additional, ^{17}O-enriched oxygen source that is incorporated into sulfate during pyrite oxidation.

We first consider atmospheric inputs. Many oxygen-bearing gases carry positive ^{17}O anomalies that can be transferred to sulfate in the atmosphere. For instance, aqueous-phase SO_2 oxidation by ^{17}O-enriched H_2O_2 or O_3 in the atmosphere generates sulfate in rainwater and aerosols with positive $\Delta'^{17}O$ values (41, 42). It is therefore possible that aerosol and/or rainwater inputs contribute to observed riverine sulfate signals. However, although correct in the required $\Delta'^{17}O$ directionality, atmospheric deposition alone fails to explain our results for three reasons:

(1) According to our conservative tracer mixing model, precipitation accounts for 2.0 ± 2.5 % of fluvial sulfate in the entire sample set and only 1.0 ± 1.1 % within the TSS, where $\Delta'^{17}O$ values are highest. If we assume all pyrite oxidation-derived sulfate follows Eq. 2 with no mass-independent isotope fractionation, then mass balance considerations require precipitation-derived sulfate with $\Delta'^{17}O$ values up to $\approx$9 ‰ VSMOW (higher if any contribution by Eq. 1 is invoked). This is nearly an order of magnitude higher than measured rainwater sulfate $\Delta'^{17}O$ (41).

Still, it has previously been shown that $\approx$25 % of sulfate

in Rocky Mountain headwater streams draining sulfate-poor gneiss and granite lithologies can be sourced from atmospheric deposition in snowpack (43). However, Marsiyandi headwater stream sulfate concentrations are ≈ 20× higher than those of Ref. (43). Thus, if we assume snowpack sulfate $\Delta'^{17}O$ values are similar in the Himalaya and Rocky Mountains (i.e., 0.8 ‰ to 1.5 ‰), then mass balance considerations would require snowpack sulfate concentrations of ≈150 µM. This is an order of magnitude higher than reported Himalayan precipitation and Rocky Mountain snowpack concentrations (38, 39, 43).

(2) Riverine sulfate $\delta^{18}O$, $\delta^{34}S$, and $\Delta'^{17}O$ trends are identical during pre-monsoon and monsoon seasons despite differences in air mass trajectories, precipitation amounts, and the importance of wet vs. dry deposition. In particular, we would expect significantly lower $\Delta'^{17}O$ during the dry pre-monsoon season since atmospheric sulfate produced by gas-phase OH does not a carry mass-independent $\Delta'^{17}O$ signal (42). Similarly, if aerosol deposition were driving observed trends, then we would expect a much larger positive signal during the monsoon season when air masses cross the (heavily polluted) Indian subcontinent (41). This is not observed. Rather, for sites in which pre-monsoon and monsoon sampling can be compared directly, there exists no statistically significant seasonal difference in either sulfate $\delta^{18}O$ (May – September: -0.1 ± 2.8 ‰; $\mu \pm 1\sigma$; $n = 4$) or sulfate $\Delta'^{17}O$ (May – September: -0.002 ± 0.030 ‰; $\mu \pm 1\sigma$; $n = 3$).

(3) Fluvial sulfate concentrations and $\Delta'^{17}O$ values both decrease as MAP increases moving downstream, opposite of the expected atmospheric deposition trend. Highly erosive tributaries draining pyrite-rich TSS lithologies exhibit particularly positive $\Delta'^{17}O$ values, up to 0.180 ‰ VSMOW, despite receiving only ≈400 mm yr^{-1} MAP (Table S2). Similar to snowpack, it is possible that glacial meltwater contributes atmospheric precipitation- or aerosol-derived sulfate to headwater streams (44). However, we observe no statistical correlation between sulfate $\Delta'^{17}O$ and aerial glacier extent across our sample set ($p > 0.05$; Table S1-S2), suggesting that glacier meltwater contributions alone cannot explain observed trends. Thus, while atmospheric deposition can contribute to fluvial sulfate with positive $\Delta'^{17}O$ values (43), such contributions are likely negligible in the Marsiyandi River basin.

Marsiyandi River headwater sulfate is thus quantitatively rock-derived. The question then arises: what is the source of ^{17}O-enriched oxygen to pyrite oxidation-derived sulfate? Pyrite oxidation proceeds via 1-electron transfer steps occurring at anode sites on the mineral surface and thus involves oxygen-bearing sulfur intermediate species ($S_2O_2^{2-}$, $S_3O_6^{2-}$, SO_3^{2-}) (11). Sulfite (SO_3^{2-}), the most likely terminal precursor to sulfate, rapidly reaches isotopic equilibrium with water (46), raising the possibility that pyrite oxidation-derived sulfate ^{17}O is buffered to water regardless of the original oxygen source. However, the measured equilibrium sulfite-water ^{18}O effect (46) is significantly larger than headwater $\Delta\delta^{18}O$ values observed here (≈ 5 ‰; Fig. 2B), suggesting sulfite-water isotope equilibrium cannot explain observed $\delta^{18}O$ and $\Delta'^{17}O$ trends.

Rather, we hypothesize that ROS isotope signatures are incorporated into pyrite oxidation-derived sulfate, consistent with laboratory experimental results (10, 11, 16, 17, 22, 40). Electrochemical studies treat pyrite as a semiconductor with a sulfur anode and an iron cathode; this model states that

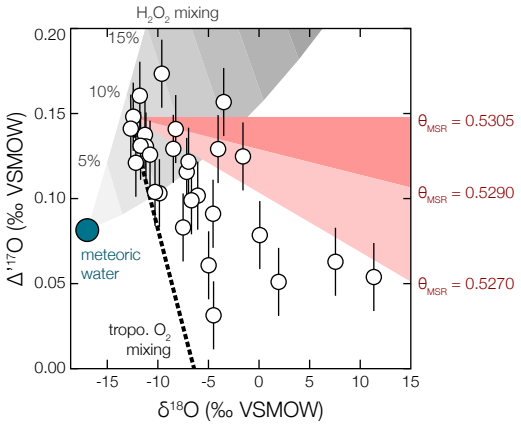

Fig. 3. Sulfate oxygen source mixing diagram. White circles are measured riverine sulfate oxygen isotope compositions (Fig. 2A); blue circle is the high-elevation headwater meteoric water composition. Gray region is a mixing array between high-elevation meteoric water and the measured range of precipitation-derived H_2O_2 compositions (24); shading represents fraction of H_2O_2 contribution. Red region is a hypothesized MSR fractionation array starting from a "primary" headwater sulfate composition; shading represents the range of possible MSR θ values (45). The black dotted line is a mixing line between the same starting composition and tropospheric O_2. The primary composition used to define this mixing space was chosen such that the majority of data fall within the bounds defined by primary sulfate, MSR fractionation, and O_2 incorporation. Measured sulfate compositions cannot be explained as a binary mixing between meteoric water and tropospheric O_2, especially in ^{17}O-enriched headwater TSS tributaries.

sulfate oxygen is quantitatively derived from H_2O or other O(−II) bearing species, whereas O_2 is reduced via ROS intermediates on iron cathode sites (22, 23). Furthermore, pyrite surfaces are almost always covered in Fe(III)-hydroxide patches (11, 47); these patches have been shown to disproportionate H_2O_2, generating O_2 and H_2O with unique isotope signatures relative to those of bulk fluid (23). If H_2O_2-derived H_2O is adsorbed onto pyrite surfaces, then these molecules could be preferentially incorporated into neighboring anode sulfur sites despite their low molarity relative to bulk water. In addition to explaining the origin of ^{17}O-enriched sulfate, this mechanism could potentially reconcile the apparent non-stoichiometric O_2 incorporation observed in isotope labeling pyrite oxidation experiments (i.e., values other than 25, 50, 75, or 100 % O_2-derived) (12, 13). That is, if isotopically labeled O_2 is reduced to H_2O via ROS intermediates on pyrite surfaces, then the apparent incorporation of this signature into sulfate would depend on the relative amount of adsorbed surface sites occupied by these molecules and would not be constrained by sulfate oxygen stoichiometry.

There are at least two pathways by which ROS incorporation could explain our observed positive sulfate $\Delta'^{17}O$ values: (1) *in situ* production of ^{17}O-enriched H_2O_2 during O_2 reduction on pyrite surfaces, or (2) delivery of atmospheric H_2O_2 to the site of pyrite oxidation, for example by rainwater (24, 25, 42). Although the mass-dependent fractionation relationships are currently not known for any step of the pyrite oxidation mechanism, the analogous H_2O_2-producing Mehler reaction has been shown to follow $\theta \approx 0.50$ (48). If O_2 reduction on pyrite surfaces follows a similar θ value as that of the Mehler reaction, then this process would generate ^{17}O-enriched H_2O_2 that could be disproportionated and incorporated into sulfate. Future research is clearly needed to constrain these

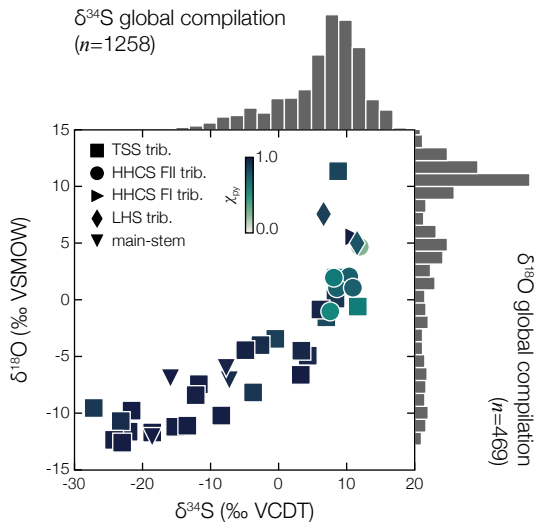

Fig. 4. Sulfate major isotope compositions. Colored points: $\delta^{18}O$ vs. $\delta^{34}S$ for all samples in Ref. (20). Symbol colors represent χ_{py} values and shapes refer to: TSS tributaries (squares), HHCS FII tributaries (circles), HHCS FI tributaries (right-pointing triangles), LHS tributaries (diamonds), and the main-stem Marsiyandi (down-pointing triangles). Histograms: literature compilations of all reported $\delta^{18}O$ and $\delta^{34}S$ values from global rivers (Table S4; Materials and Methods). Marsiyandi River basin $\delta^{18}O$ and $\delta^{34}S$ compositions span nearly the entire global range and approach global median values moving downstream.

fractionation factors.

Alternatively, it has been shown that rainwater contains up to ≈30 µM H_2O_2 with $\Delta'^{17}O$ values near 1.0 ‰ VSMOW (25). A substantial fraction of this H_2O_2 is transferred to river water; measured concentrations reach ≈150 nM (49, 50). If we assume (i) pyrite oxidation-derived sulfate oxygen is sourced from a mixture of river water and H_2O_2, (ii) rainwater H_2O_2 $\Delta'^{17}O$ values reported in the literature (25) are generally representative, and (iii) disproportionation and incorporation into sulfate molecules does not impart a mass-independent anomaly (12), then atmospherically derived H_2O_2 could contribute 7 to 15 % of sulfate oxygen in Marisyandi headwaters (Fig. 3). This result satisfies both $\delta^{18}O$ and $\Delta'^{17}O$ observations. Still, it remains unclear how and to what extent rainwater H_2O_2 would survive to the site of pyrite oxidation; while this estimate based on the limited existing literature ROS $\Delta'^{17}O$ data (24) appears reasonable, we emphasize that we do not quantitatively trust these results.

Regardless of the exact delivery mechanism invoked, pyrite oxidation-derived sulfate oxygen in mountainous rivers must be sourced primarily from meteoric water with supplemental contributions from a ^{17}O-enriched source. Electrochemical models and limited $\Delta'^{17}O$ measurements suggest this source is likely H_2O_2, but other ROS (e.g., $O_2^{\bullet-}$, $OH^{\bullet}$) or oxidants (e.g., NO_3^-) containing positive ^{17}O anomalies (51) could instead be driving observed signals. Future work is needed to provide detailed constraints on the importance of each of these species and pathways.

Downstream Evolution and Implications for Global Sulfur Budgets. Moving downstream, riverine sulfate becomes enriched in ^{34}S and ^{18}O and loses its positive ^{17}O anomaly. This transition occurs within tributaries draining the TSS and is therefore unlikely to result from changes in weathering lithology (Fig. S1). Rather, microbial sulfate reduction (MSR) is more active in lower elevation, warmer catchments overlain by thicker, organic-rich soils. In particular, hyporheic zones—anoxic bank and bed sediments that are in hydrologic contact with river water (52)—are known to host highly active sulfate-reducing bacterial communities (53) and are thus a likely locus of MSR in the Marsiyandi River basin. MSR followed by sulfide precipitation or outgassing will increase residual sulfate $\delta^{34}S$ and $\delta^{18}O$ values independent of the original sulfate source; the observed isotope fractionations are consistent in magnitude and direction with laboratory studies (54) and with previous field measurements (55). This mechanism is further supported by the strong positive relationships between local MAT and both sulfate $\delta^{34}S$ ($p = 2.9 \times 10^{-7}$; $R^2 = 0.53$) and $\delta^{18}O$ values ($p = 1.6 \times 10^{-6}$; $R^2 = 0.49$; Table S1, S2).

Resulting biogenic sulfide could be lost via H_2S outgassing from anoxic soils or retained locally as secondarily precipitated sulfide minerals and/or organic sulfur (56). For example, previous studies have utilized a network of bore holes in a temperature, first order stream to show that MSR can lead to an order-of-magnitude H_2S supersaturation with respect to sulfide mineral precipitation (FeS and FeS_2) in anoxic river bank sediments (53). The interpretation that sulfate reduction and subsequent loss is driving observed isotope trends is supported by strong negative correlations between sulfate concentration and both sulfate $\delta^{34}S$ ($p = 1.6 \times 10^{-10}$; $R^2 = 0.69$) and $\delta^{18}O$ values ($p = 3.6 \times 10^{-9}$; $R^2 = 0.63$; Table S1). If glacially carved valleys are being actively infilled by sediment in this region, then non-steady-state growth of secondarily precipitated sulfur reservoirs could exacerbate observed downstream sulfate isotope enrichments; this is likely occurring given such large $\delta^{34}S$ variability observed here (Fig. 4). However, in general, non-steady-state conditions are not required to explain progressive $\delta^{34}S$ enrichment as long as the standing stock of secondarily precipitated sulfur is significantly ^{34}S-depleted relative to inflowing sulfate (56), as would be expected with MSR (54, 55).

Interestingly, Marsiyandi River sulfate $\delta^{34}S$ and $\delta^{18}O$ values span nearly the entire range measured in rivers across the globe (Fig. 4). The majority of this isotope variability occurs within a single lithologic unit, the TSS, despite all evidence to suggest sulfate is quantitatively derived from pyrite oxidation. This observation implies that riverine sulfate $\delta^{34}S$ compositions are an insufficient conservative tracer to estimate pyrite vs. evaporite weathering contributions to global fluvial sulfate export (20, 56, 57). In the TSS alone, MSR appears to increase $\delta^{34}S$ by ≈30 ‰ within consistently pyrite-dominated lithology; this would traditionally be interpreted as a shift from pyrite-dominated to evaporite-dominated weathering (57). Furthermore, downstream Marsyandi River tributary isotope compositions approach median values for global data sets, suggesting that global $\delta^{34}S$ and $\delta^{18}O$ distributions may more strongly reflect MSR intensity and secondary sulfur storage in floodplains than weathering lithology.

Sulfate $\Delta'^{17}O$ trends corroborate the importance of MSR and secondary sulfur recycling in downstream catchments. Although the mass-dependent relationship describing MSR (θ_{MSR}) is poorly constrained, it likely lies between 0.5270 and 0.5305 (45). If we assume pyrite oxidation throughout the catchment generates primary sulfate with an isotope composition similar to that observed in high-elevation headwater

streams, then fractionation by MSR would lead to the observed increase in $\delta^{18}O$ as well as a slight decrease in $\Delta'^{17}O$ of residual sulfate (Fig. 3). Still, most downstream tributary data fall below the MSR fractionation line and imply secondary incorporation of ^{17}O-depleted oxygen into sulfate, most likely from O_2.

Sulfide generated by MSR can be reoxidized either biotically or abiotically. Aerobic, chemolithoautotrophic sulfide oxidizing bacteria (SOB) are known to rapidly oxidize sulfide to sulfate in the presence of O_2 (58). However, aerobic SOB likely utilize an electron transport chain rather than an oxygenase enzyme (59); resulting sulfate oxygen atoms are thus exclusively derived from H_2O and not from O_2 directly (60). Alternatively, abiotic H_2S oxidation, while kinetically slower than oxidation by SOB (58), would directly incorporate O_2 and could explain observed downstream trends. This mechanism—MSR followed by secondary H_2S oxidation and abiotic O_2 incorporation—additionally reconciles our data with previous riverine sulfate $\Delta'^{17}O$ observations. Specifically, Mississippi River sulfate in Baton Rouge, Louisiana, USA displays a negative mean $\Delta'^{17}O$ of -0.091 ± 0.043 ‰ VSMOW ($n = 41$), which was previously interpreted to reflect tropospheric O_2 contributions during pyrite oxidation (61). We instead interpret this result as reflecting continued secondary sulfur recycling, although the potential for alternative sulfate sources and anthropogenic inputs in the Mississippi River cannot be discounted (61).

If the mechanism proposed here is true more generally, then the locus of O_2 incorporation into sulfate occurs not in erosive, pyrite-rich headwaters but rather during secondary sulfur recycling in lowland floodplains. This difference could carry implications for sulfate ^{17}O compositions through geologic time.

Conclusion and Implications for Earth History. The utility of sulfate $\Delta'^{17}O$ as a paleo-pO_2 tracer is predicated on tropospheric O_2 incorporation via oxidative pyrite weathering. In this study, we targeted highly erosive rivers draining pyrite-rich shale lithologies to isolate the ^{17}O signature of pyrite oxidation-derived sulfate; results under modern conditions suggest a complex reaction network that does not directly incorporate O_2. However, O_2 is the only major atmospheric species that carries a negative ^{17}O anomaly; observed $\Delta'^{17}O$ values in Precambrian sulfate-bearing rocks therefore require atmospheric O_2 incorporation into sulfate precursors (3–8, 14, 15). Here we hypothesize that such incorporation may occur during secondary sulfur recycling in floodplains; this mechanism predicts that floodplain area could act as an additional, previously unrecognized control on sulfate ^{17}O composition. Still, open questions remain regarding the interpretation of geologic sulfate $\Delta'^{17}O$ records, including the dependence of ROS ^{17}O compositions on pO_2/pCO_2 and the implications for paleoatmospheric compositions. Answering these questions will require mechanistic studies in modern settings in addition to new, high-resolution $\Delta'^{17}O$ measurements of geologic sulfate throughout the Phanerozoic Eon.

Materials and Methods

The materials and methods are summarized here; further details are provided in the Supporting Information.

Isotope Measurements and Data Reporting. Site location and sample collection details, as well as major ion, $^{18}O/^{16}O$, and $^{34}S/^{32}S$ analytical procedures, have been described previously (20, 29, 33–35). Sulfate $^{17}O/^{16}O$ ratios were measured by laser fluorination by F_2 coupled with isotope ratio mass spectrometry (IRMS) following Ref. (62). Uncertainty ($\pm 1\sigma$) was taken as the long-term reproducibility of a suite of primary sulfate standards ($\sigma = 0.016$). Isotope ratios are reported in conventional delta notation:

$$\delta^i O = \left(\frac{^{i/16}R_{sample}}{^{i/16}R_{standard}} - 1 \right) \times 1000‰, \quad [3]$$

where $i = 17, 18$ is the isotope of interest, $^{i/16}R$ is the $^iO/^{16}O$ ratio, and Vienna Standard Mean Ocean Water (VSMOW) is the reference standard. $\delta^{34}S$ is similarly reported using Vienna Canyon Diablo Triolite (VCDT) as the reference standard. To quantify small deviations from the expected mass-dependent $\delta^{17}O$-$\delta^{18}O$ relationship, $^{17}O/^{16}O$ ratios are reported as

$$\Delta'^{17}O = \left[\ln\left(\frac{\delta^{17}O}{1000} + 1 \right) - \theta_{RL} \ln\left(\frac{\delta^{18}O}{1000} + 1 \right) \right] \times 1000‰, \quad [4]$$

where $\theta_{RL} = 0.5305$ is the high-temperature equilibrium reference line mass law (63) and $'$ indicates logarithmic notation (64). Isotope offsets between sulfate and concomitant water are reported as

$$\Delta\delta^{18}O = \delta^{18}O_{SO_4{}^{2-}} - \delta^{18}O_{H_2O}. \quad [5]$$

and

$$\Delta\Delta'^{17}O = \Delta'^{17}O_{SO_4{}^{2-}} - \Delta'^{17}O_{H_2O}. \quad [6]$$

All major ion concentrations and sulfate isotope compositions are reported in Table S1.

Geospatial Analysis. Geospatial data were analyzed using ArcGis Desktop v10.6 (ESRI Corporation); results are reported in Table S2. Catchment areas and geomorphic parameters upstream of each sampling location were calculated using the NASA Shuttle Radar and Topography Mission global digital elevation model v3.0 (1 arc-second resolution). Glacier extent was calculated using the Randolph Glacier Inventory v6.0. Mean annual precipitation (MAP) and mean annual temperature (MAT) were calculated using the WorldClim v2 global climate database (30 second resolution) (65). Local elevation, slope, MAT, and MAP for each sample were taken as the value of the raster pixel underlying each sampling location. Catchment-averaged elevation, slope, MAP, and MAT were calculated as the mean value for all pixels within a given catchment area. Main-stem distance, elevation, and MAT profiles (Fig. 1B) were generated using the flow-accumulation river network and underlying raster pixels. Sample downstream distances were calculated as the main-stem path length from the headwater source to the main-stem point nearest to each sample location.

Weathering Lithology Mixing Model. For each sample, the relative proportions of solutes derived from weathering of different end-member lithologies were estimated using a conservative tracer mixing model. The end members considered in this model were: dolomite, evaporites, gneiss/granite, limestone, and shale. Although evaporite lithologies in general—and gypsum in particular—have not been reported in the Marsiyandi basin (26), we nonetheless included them in the model since their presence would add non-pyrite-derived $SO_4{}^{2-}$. Our calculated pyrite-derived $SO_4{}^{2-}$ contributions are thus minimum estimates. The conservative tracers considered in this model were: Ca^{2+}, K^+, Mg^{2+}, Na^+, Cl^-, $SO_4{}^{2-}$, and the constraint that all fractional contributions sum to unity. This model was solved using a Monte Carlo approach similar to that of Ref. (56). In addition to end-member contributions to each sample, this approach estimated *a posteriori* end-member conservative tracer ranges. Finally, the fraction of pyrite-derived $SO_4{}^{2-}$ in each sample, termed χ_{py}, was calculated as the relative proportion of shale weathering in that sample multiplied by the *a posteriori* $SO_4{}^{2-}$ concentration for the shale end member. *A priori* and *a posteriori* end-member conservative tracer ranges are reported in Table S3.

Major Isotope Compilation and Data Analysis

All published fluvial sulfate $\delta^{34}S$ and $\delta^{18}O$ compositions, along with paired water $\delta^{18}O$ where available, were compiled from Refs.

(18–20, 57, 61, 66–70) (Table S4). Regression slopes were calculated using either weighted least squares regression if the ordinate is known perfectly (i.e., downstream distance; Fig. S1) or reduced major axis regression if the ordinate is known to contain uncertainty (i.e., isotope cross plots). Reported p values are the probability that regression slopes are statistically equal to zero and regressions with $p \leq 0.05$ are deemed significant. See Ref. (71) for regression details and equations.

ACKNOWLEDGMENTS. We thank Julien Foriel for laboratory assistance, Kevin Sutherland for helpful discussions on early versions of the manuscript, as well as the editor and two anonymous reviewers whose comments greatly improved the overall strength and clarity of this paper. This research was supported by NSF EAGER grant number EAR1839341, ACS PRF grant number 59455-ND2 (both to J.D.H. and D.T.J.) and NSF MGG grant number OCE-1821958 (to D.T.J.).

1. Thiemens MH (2006) History and applications of mass-independent isotope effects. *Annu. Rev. Earth Planet. Sci.* 34:217–262.
2. Lyons TW, Reinhard CT, Planavsky NJ (2014) The rise of oxygen in earth's early ocean and atmosphere. *Nature* 506:307–315.
3. Bao H, et al. (2000) Anomalous ^{17}O compositions in massive sulphate deposits on the earth. *Nature* 406:176–179.
4. Bao H, Lyons J, Zhou C (2008) Triple oxygen isotope evidence for elevated CO_2 levels after a neoproterozoic glaciation. *Nature* 453:504–506.
5. Bao H, Fairchild IJ, Wynn PM, Spötl C (2009) Stretching the envelope of past surface environments: Neoproterozoic glacial lakes from svalbard. *Science* 323:119–122.
6. Cao X, Bao H (2013) Dynamic model constraints on oxygen-17 depletion in atmospheric O_2 after a snowball earth. *Proc. Nat. Acad. Sci.* 110:14546–14550.
7. Crockford PW, et al. (2018) Triple oxygen isotope evidence for limited mid-proterozoic primary productivity. *Nature* 559:613–616.
8. Crockford PW, et al. (2019) Claypool continued: Extending the isotopic record of sedimentary sulfate. *Chem. Geol.* 513:200–225.
9. Yung YL, Lee AY, Irion FW, DeMore WB, Wen J (1997) Carbon dioxide in the atmosphere: Isotopic exchange with ozone and its use as a tracer in the middle atmosphere. *J. Geophys. Res. Atmos.* 102:10857–10866.
10. Williamson MA, Rimstidt JD (1994) The kinetics and electrochemical rate-determining step of aqueous pyrite oxidation. *Geochim. Cosmochim. Ac.* 58:5443–5454.
11. Rimstidt JD, Vaughan DJ (2003) Pyrite oxidation: A state-of-the-art assessment of the reaction mechanism. *Geochim. Cosmochim. Ac.* 67:873–880.
12. Kohl I, Bao H (2011) Triple-oxygen-isotope determination of molecular oxygen incorporation in sulfate produced during abiotic pyrite oxidation (ph = 2–11). *Geochim. Cosmochim. Ac.* 75:1785–1798.
13. Balci N, Shanks III WC, Mayer B, Mandernack KW (2007) Oxygen and sulfur isotope systematics of sulfate produced by bacterial and abiotic oxidation of pyrite. *Geochim. Cosmochim. Ac.* 71:3796–3811.
14. Crockford PW, et al. (2016) Triple oxygen and multiple sulfur isotope constraints on the evolution of the post-marinoan sulfur cycle. *Earth Planet. Sci. Lett.* 435:74–83.
15. Hodgskiss MS, Crockford PW, Peng Y, Wing BA, Horner TJ (2019) A productivity collapse to end earth?s great oxidation. *Proceedings of the National Academy of Sciences* 116(35):17207–17212.
16. Reedy BJ, Beattie JK, Lowson RT (1991) A vibrational spectroscopic ^{18}O tracer study of pyrite oxidation. *Geochim. Cosmochim. Ac.* 55:1609–1614.
17. Holmes PR, Crundwell FK (2000) The kinetics of the oxidation of pyrite by ferric ions and dissolved oxygen: An electrochemical study. *Geochim. Cosmochim. Ac.* 64:263–274.
18. Calmels D, Gaillardet J, Brenot A, France-Lanord C (2007) Sustained sulfide oxidation by physical erosion processes in the mackenzie river basin: Climatic perspectives. *Geology* 35:1003–1006.
19. Das A, Chung CH, You CF (2012) Disproportionately high rates of sulfide oxidation from mountainous river basins of taiwan orogeny: Sulfur isotope evidence. *Geophys. Res. Lett.* 39:L12404.
20. Turchyn AV, Tipper ET, Galy A, Lo JK, Bickle MJ (2013) Isotope evidence for secondary sulfide precipitation along the marsyandi river, nepal, himalayas. *Earth Planet. Sci. Lett* 374:36–46.
21. Gu X, et al. (2020) Chemical reactions, porosity, and microfracturing in shale during weathering: The effect of erosion rate. *Geochimica et Cosmochimica Acta* 269:63–100.
22. Lefticariu L, Schimmelmann A, Pratt LM, Ripley EM (2007) Oxygen isotope partitioning during oxidation of pyrite by H_2O_2 and its dependence on temperature. *Geochim. Cosmochim. Ac.* 71:5072–5088.
23. Schoonen MA, Harrington AD, Laffers R, Strongin DR (2010) Role of hydrogen peroxide and hydroxyl radical in pyrite oxidation by molecular oxygen. *Geochimica et Cosmochimica Acta* 74(17):4971–4987.
24. Savarino J, Thiemens MH (1999) Analytical procedure to determine both δ^{18}O and δ^{17}O of h_2o_2 in natural water and first measurements. *Atmos. Environ.* 33:3683–3690.
25. Savarino J, Thiemens MH (1999) Mass-independent oxygen isotope (^{16}o, ^{17}o, ^{18}o) fractionation found in h_x, o_x reactions. *J. Phys. Chem. A* 103:9221–9229.
26. Bordet P, et al. (1971) *Recherches Géologiques dans l'Himalaya du Népal, Région de la Thakkhola*. (Éd. du Centre Nat. de la Recherche Scientif.).
27. Coleman M (1996) Orogen-parallel and orogen-perpendicular extension in the central nepalese himalayas. *Geol. Soc. Am. Bull.* 108:1594–1607.
28. Searle MP, Godin L (2003) The south tibetan detachment and the manaslu leucogranite: A structural reinterpretation and restoration of the annapurna-manaslu himalaya, nepal. *J. Geol.* 111:505–523.
29. Tipper ET, et al. (2006) The short term climatic sensitivity of carbonate and silicate weathering fluxes: Insight from seasonal variations in river chemistry. *Geochim. Cosmochim. Ac.* 70:2737–2754.
30. Bookhagen B, Burbank DW (2010) Toward a complete himalayan hydrological budget: Spatiotemporal distribution of snowmelt and rainfall and their impact on river discharge. *J.Geophys. Res. Earth Surf.* 115:F03019.
31. Le Fort P (1975) Himalayas: The collided range. present knowledge of the continental arc. *Am. J. Sci.* 275:1–44.
32. Sharp Z, Wostbrock J, Pack A (2018) Mass-dependent triple oxygen isotope variations in terrestrial materials. *Geochem. Perspect. Lett.* 7:27–31.
33. Becker JA, Bickle MJ, Galy A, Holland TJ (2008) Himalayan metamorphic CO_2 fluxes: Quantitative constraints from hydrothermal springs. *Earth Planet. Sci. Lett.* 265:616–629.
34. Bickle MJ, et al. (2005) Relative contributions of silicate and carbonate rocks to riverine sr fluxes in the headwaters of the ganges. *Geochim. Cosmochim. Ac.* 69:2221–2240.
35. Tipper ET, Galy A, Bickle MJ (2008) Calcium and magnesium isotope systematics in rivers draining the himalaya-tibetan-plateau region: Lithological or fractionation control? *Geochim. Cosmochim. Ac.* 72:1057–1075.
36. Hemingway JD, et al. (2019) Glacier meltwater and monsoon precipitation drive upper ganges basin dissolved organic matter composition. *Geochim. Cosmochim. Ac.* 244:216–228.
37. Evans MJ, Derry LA, Anderson SP, France-Lanord C (2001) Hydrothermal source of radiogenic sr to himalayan rivers. *Geology* 29:803–806.
38. Galy A, France-Lanord C (1999) Weathering processes in the ganges–brahmaputra basin and the riverine alkalinity budget. *Chem. Geol.* 159:31–60.
39. Galy A, France-Lanord C, Derry LA (1999) The strontium isotopic budget of himalayan rivers in nepal and bangladesh. *Geochim. Cosmochim. Ac.* 63:1905–1925.
40. Fowler T, Holmes P, Crundwell F (1999) Mechanism of pyrite dissolution in the presence of *Thiobacillus ferrooxidans*. *Appl. Environ. Microbiol.* 65:2987–2993.
41. Lee CCW, Savarino J, Thiemens MH (2001) Mass independent oxygen isotopic composition of atmospheric sulfate: Origin and implications for the present and past atmosphere of earth and mars. *Geophys. Res. Lett.* 28:1783–1786.
42. Savarino J, Lee CC, Thiemens MH (2000) Laboratory oxygen isotopic study of sulfur (iv) oxidation: Origin of the mass-independent oxygen isotopic anomaly in atmospheric sulfates and sulfate mineral deposits on earth. *J. Geophys. Res. Atmos.* 105:29079–29088.
43. Johnson CA, Mast MA, Kester CL (2001) Use of ^{17}O/^{16}O to trace atmospherically-deposited sulfate in surface waters: A case study in alpine watersheds in the rocky mountains. *Geophysical research letters* 28:4483–4486.
44. Duan K, Thompson L, Yao T, Davis M, Mosley-Thompson E (2007) A 1000 year history of atmospheric sulfate concentrations in southern asia as recorded by a himalayan ice core. *Geophysical Research Letters* 34:L01810.
45. Waldeck A, et al. (2019) Deciphering the atmospheric signal in marine sulfate oxygen isotope composition. *Earth Planet. Sci. Lett.* 522:12–19.
46. Wankel SD, Bradley AS, Eldridge DL, Johnston DT (2014) Determination and application of the equilibrium oxygen isotope effect between water and sulfite. *Geochim. Cosmochim. Ac.* 125:694–711.
47. Becker U, Rosso KM, Hochella Jr MF (2001) The proximity effect on semiconducting mineral surfaces: a new aspect of mineral surface reactivity and surface complexation theory? *Geochimica et Cosmochimica Acta* 65:2641–2649.
48. Helman Y, Barkan E, Eisenstadt D, Luz B, Kaplan A (2005) Fractionation of the three stable oxygen isotopes by oxygen-producing and oxygen-consuming reactions in photosynthetic organisms. *Plant Physiology* 138:2292–2298.
49. Cooper WJ, Lean D, Carey J (1989) Spatial and temporal patterns of hydrogen peroxide in lake waters. *Can. J. Fish. Aquat. Sci.* 46:1227–1231.
50. Mostofa KM, Sakugawa H (2009) Spatial and temporal variations and factors controlling the concentrations of hydrogen peroxide and organic peroxides in rivers. *Environ. Chem.* 6:524–534.
51. Michalski G, Scott Z, Kabiling M, Thiemens MH (2003) First measurements and modeling of δ17o in atmospheric nitrate. *Geophysical Research Letters* 30.
52. Kiel BA, Cardenas MB (2014) Lateral hyporheic exchange throughout the mississippi river network. *Nature Geoscience* 7:1–5.
53. Baier MA, Dahm CN, Valett HM (1999) Acetate retention and metabolism in the hyporheic zone of a mountain stream. *Limnology & Oceanography* 44:1530–1539.
54. Leavitt WD, Halevy I, Bradley AS, Johnston DT (2013) Influence of sulfate reduction rates on the phanerozoic sulfur isotope record. *Proc. Nat. Acad. Sci.* 110:11244–11249.
55. Masterson A, Alperin MJ, Berelson WM, Johnston DT (2018) Interpreting multiple sulfur isotope signals in modern anoxic sediments using a full diagenetic model (california-mexico margin: Alfonso basin). *American Journal of Science* 318:459–490.
56. Torres MA, et al. (2016) The acid and alkalinity budgets of weathering in the andes–amazon system: Insights into the erosional control of global biogeochemical cycles. *Earth Planet. Sci. Lett.* 450:381–391.
57. Burke A, et al. (2018) Sulfur isotopes in rivers: Insights into global weathering budgets, pyrite oxidation, and the modern sulfur cycle. *Earth Planet. Sci. Lett* 496:168–177.
58. Luther GW, et al. (2011) Thermodynamics and kinetics of sulfide oxidation by oxygen: a look at inorganically controlled reactions and biologically mediated processes in the environment. *Frontiers in microbiology* 2:62.
59. Van Stempvoort D, Krouse H (1994) Controls of δ18o in sulfate: Review of experimental data and application to specific environments in *Environmental Geochemistry of Sulfide Oxidation*, eds. Alpers C, Blowes D. (ACS Publications, Washington, D.C.).
60. Suzuki I (1965) Incorporation of atmospheric oxygen-18 into thiosulfate by the sulfur-oxidizing enzyme of thiobacillus thiooxidans. *Biochimica et Biophysica Acta* 110:97–101.
61. Killingsworth BA, Bao H, Kohl IE (2018) Assessing pyrite-derived sulfate in the mississippi river with four years of sulfur and triple-oxygen isotope data. *Environ. sci. Technol.* 52:6126–6136.

62. Cowie BR, Johnston DT (2016) High-precision measurement and standard calibration of triple oxygen isotopic compositions (δ^{18}O, Δ'^{17}O) of sulfate by F_2 laser fluorination. *Chem. Geol.* 440:50–59.
63. Young ED, Galy A, Nagahara H (2002) Kinetic and equilibrium mass-dependent isotope fractionation laws in nature and their geochemical and cosmochemical significance. *Geochim. Cosmochim. Ac.* 66:1095–1104.
64. Miller MF (2002) Isotopic fractionation and the quantification of ^{17}17O anomalies in the oxygen three-isotope system: An appraisal and geochemical significance. *Geochim. Cosmochim. Ac.* 66:1881–1889.
65. Fick SE, Hijmans RJ (2017) Worldclim 2: new 1-km spatial resolution climate surfaces for global land areas. *Int. J. Climatol.* 37:4302–4315.
66. Robinson BW, Bottrell SH (1997) Discrimination of sulfur sources in pristine and polluted new zealand river catchments using stable isotopes. *Appl. Geochem.* 12:305–319.
67. Karim A, Veizer J (2000) Weathering processes in the indus river basin: implications from riverine carbon, sulfur, oxygen, and strontium isotopes. *Chem. Geol.* 170:153–177.
68. Otero N, Soler A, Canals À (2008) Controls of δ^{34}S and δ^{18}O in dissolved sulphate: learning from a detailed survey in the llobregat river (spain). *Appl. Geochem.* 23:1166–1185.
69. Li SL, Chetelat B, Yue F, Zhao Z, Liu CQ (2014) Chemical weathering processes in the yalong river draining the eastern tibetan plateau, china. *J. Asian Earth Sci.* 88:74–84.
70. Hindshaw RS, Heaton TH, Boyd ES, Lindsay MR, Tipper ET (2016) Influence of glaciation on mechanisms of mineral weathering in two high arctic catchments. *Chem. Geol.* 420:37–50.
71. Rayner J (1985) Linear relations in biomechanics: The statistics of scaling functions. *J. Zool.* 206:415–439.